ISSN 0023-1584, Kinetics and Catalysis, 2010, Vol. 51, No. 5, pp. 743–753. © Pleiades Publishing, Ltd., 2010.
Original Russian Text © A.N. Il'ichev, D.P. Shashkin, T.I. Khomenko, Z.T. Fattakhova, V.N. Korchak, 2010, published in Kinetika i Kataliz, 2010, Vol. 51, No. 5, pp. 769–779.

Structure and Surface Properties of ZrO_2, CeO_2, and $Zr_{0.5}Ce_{0.5}O_2$ Prepared by a Microemulsion Method According to X-Ray Diffraction, TPR, and EPR Data

A. N. Il'ichev, D. P. Shashkin, T. I. Khomenko, Z. T. Fattakhova, and V. N. Korchak

Semenov Institute of Chemical Physics, Russian Academy of Sciences, Moscow, 119991 Russia

e-mail: Ilichev-an@mail.ru

Received December 22, 2009

Abstract—It was established by X-ray diffraction, TPR, and EPR that microemulsion (m.e.) synthesis yields the binary oxides ZrO_2(m.e.) and CeO_2(m.e.) and the mixed oxide $Zr_{0.5}Ce_{0.5}O_2$(m.e.) in the form of a tetragonal, cubic, and pseudocubic phase, respectively, having crystallite sizes of 5–6 nm. The bond energy of surface oxygen in the (m.e.) samples is lower than in their analogues prepared by pyrolysis. Hydrogen oxidation on the oxides under study occurs at higher temperatures than CO oxidation. ZrO_2(m.e.) and CeO_2(m.e.) are active in O_2^- formation during NO + O_2 adsorption, while CeO_2 is active during CO + O_2 adsorption, too. However, its amount here is one-half to one-third its amount in the pyrolysis-prepared samples, signifying a reduced number of active sites, which are Zr^{4+} and Ce^{4+} coordinatively unsaturated cations and Me^{4+}–O^{2-} pairs. O_2^- radical anions are stabilized in the coordination sphere of Zr^{4+} coordinatively unsaturated cations via ionic bonding, and in the sphere of Ce^{4+} cations, via covalent bonding. Ionic bonds are stronger than ionic–covalent bonds and do not depend on the ZrO_2 phase composition. $Zr_{0.5}Ce_{0.5}O_2$ is inactive in these reactions because of the strong interaction of Zr and Ce cations. It is suggested that $Ce^{(4+\beta)+}$ coordinatively unsaturated cations exist on its surface, and their acid strength is lower than that of Zr^{4+} and Ce^{4+} cations in ZrO_2 and CeO_2, according to the order $ZrO_2 > CeO_2 \geq Zr_{0.5}Ce_{0.5}O_2$. Neither TPR nor adsorption of probe molecules revealed Zr cations on the surface of the mixed oxide.

DOI: 10.1134/S0023158410050174

ZrO_2, CeO_2, and $Ce_xZr_{1-x}O_2$ oxide systems containing acid–base sites are widely used in heterogeneous catalysis. For example, ZrO_2 is active in hydrogenation of CO [1], olefins [2], and dienes [3]. CeO_2 carries out the reactions of ethane oxidehydrogenation [4], steam reforming [5], and reduction of nitrogen oxides [6]. The high thermal stability of ZrO_2 and the ability of CeO_2 to disperse supported oxides and metals and to store oxygen have been employed in creating $Ce_xZr_{1-x}O_2$ supports for catalysts that carry out NO_x, CO, and hydrocarbon neutralization reactions [7, 8] and low-temperature oxidation of CO with oxygen in excess hydrogen [9–11].

Studies into catalytic properties of nanostructured ZrO_2, CeO_2, and $Ce_xZr_{1-x}O_2$ are now underway. Some researchers noted their higher reactivities compared to their analogues prepared by pyrolysis of nitrate salts or hydroxides [12]. Such oxides are prepared by thermolysis of an organometallic precursor in a flow-through reactor [13, 14], sol–gel technology [15–17], and microemulsion technology [18]. They have high specific surface areas (100–200 m^2/g) and are characterized by high crystallite size homogeneity with an average crystallite size of 3–5 nm, as distinct from their analogues having small specific surface areas (0.3–20 m^2/g) prepared by high-temperature decomposition [19] or mechanochemically [20].

However, nanometer particle sizes do not ensure an enhancement or at least retention of activity, which is due to the existence of coordinatively unsaturated surface sites. This is for the reason that oxides having crystallite sizes less than 10 nm are synthesized under nonequilibrium conditions where thermodynamically stable and metastable phases can both be formed in various proportions and can have various surface activities, as shown for ZrO_2 [13].

In this connection, it was of interest to compare the activities and surface properties (namely, the reactivity of surface oxygen, amount of coordinatively unsaturated cations, and acidity of cations) of ZrO_2, CeO_2, and $Ce_xZr_{1-x}O_2$ nanostructured oxides with their analogues prepared by pyrolysis.

For this purpose, we used electron-transfer reactions in NO + O_2 joint adsorption on ZrO_2 [21, 22] and CeO_2 [23] and in CO + O_2 adsorption on CeO_2 [24, 25]. These reactions were shown earlier to occur on coordinatively unsaturated ions of samples synthesized by pyrolysis which have crystallite sizes greater than 10 nm. They are sensitive to oxidation/reduction treatment parameters and to the composition and

nature of adsorbates and supported metal cations. Therefore, electron-transfer reactions are useful as test reactions for tracing changes in the properties of adsorbed oxygen and coordinatively unsaturated surface sites of oxides.

In this work, ZrO_2, CeO_2, and $Zr_{0.5}Ce_{0.5}O_2$ samples were prepared using microemulsion technology. Their phase composition and crystallite sizes have been studied by powder X-ray diffraction, and the reactivity of surface oxygen in hydrogen oxidation was studied in the TPR mode. EPR spectroscopy was used to study electron-transfer reactions on test samples during $NO + O_2$ and $CO + O_2$ adsorption, oxygen adsorption, and low-temperature NO adsorption on coordinatively unsaturated sites as dependent on the oxidation/reduction and vacuum treatment of the test samples.

EXPERIMENTAL

Binary and mixed oxides (ZrO_2, CeO_2, and $Zr_{0..5}Ce_{0..5}O_2$) were prepared using microemulsion technology (m.e.), as described in [18], from Aldrich reagents. Emulsions were prepared by combining aqueous solutions of individual salts ($ZrOCl_2 \cdot 8H_2O$ and $Ce(NO_3)_3 \cdot 6H_2O$) or their mixtures (with the cation ratio Zr : Ce = 1) and tetramethylammonium hydroxide pentahydrate with an organic solution containing hexane, hexanol, and the surfactant Triton X-100. The salts were reacted with tetramethylammonium while emulsion was stirred for 24 h. Reaction products were separated by centrifugation, washed with methanol, dried at room temperature, heated in air at a constant heating rate of 2 K/min to 500°C, and exposed to this temperature for 2 h.

Zirconia and ceria samples were also prepared by pyrolysis of nitrates ($ZrO(NO_3)_2$ and $Ce(NO_3)_3$(p.n.) and hydrated $ZrO_2 \cdot nH_2O$(p.h.) via heating them in air under the conditions specified above. Hydrated zirconia $ZrO_2 \cdot nH_2O$ was precipitated with ammonia from an aqueous solution of $ZrOCl_2 \cdot 8H_2O$ followed by centrifuging, single water washing, and drying the precipitate in air at 100°C according to [26].

BET specific surface areas were determined chromatographically from thermal argon desorption. The accuracy of the method was 20%.

The phase composition of oxides was studied using powder X-ray diffraction on a DRON-3M diffractometer in the 2θ range from 8° to 70° using a CuK_α anode with a nickel filter at a voltage of 30 kV and current of 25 A. The detector rotation speed was 2 deg/min. All calculations and spectra processing were performed using computer software. The instrument was calibrated against a SiO_2 (α-quartz) powder having the interplanar spacing $d = 1.818$ Å and *hkl* (112).

For EPR studies, a 50-mg portion of a sample was placed in a quartz EPR tube, evacuated to $P = 2 \times 10^{-4}$ Pa, and heated for 1 h by raising temperature from 20 to 500°C. Then, the sample was oxidized with oxygen at 500°C and $p = 7 \times 10^2$ Pa for 30 min, cooled with O_2 to 20°C, and evacuated. Following this treatment, gases were adsorbed on the oxidized sample at a chosen temperature and EPR spectra were recorded.

EPR spectra in the X-band range were recorded at 20 to −196°C on an EPR-V spectrometer equipped with a Diapazon thermal attachment. The spectrometer was calibrated against 2,2-diphenyl-1-picrylhydrazyl ($g = 2.0036$) and a Mn^{2+}/MgO standard. The amount of paramagnetic particles was derived from EPR spectra after double integration and comparison with the $CuSO_4 \cdot 5H_2O$ reference. The measurement precision in this case was 20%.

Probe gases (NO, CO, O_2, and H_2) were prepared using routine procedures as described in [27]. They were admitted to a sample through a trap filled with liquid nitrogen to remove CO_2 and H_2O uncontrolled impurities.

Temperature-programmed reduction studies were carried out on 0.1-g samples in 6% H_2/Ar flowing at a rate of 100 ml/min with a thermal-conductivity detector. Heating was performed in the range 20–500°C at 12 K/min. Prior to an experiment, samples were calcined in flowing air at 500°C for 1 h. Hydrogen uptake was derived from the TPR peak area with an accuracy of ~10%.

RESULTS

Structure of Samples as Determined by X-Ray Diffraction

Figure 1a (spectrum *1*) shows the X-ray diffraction pattern of the ZrO_2 sample prepared by the microemulsion method (ZrO_2(m.e.)). According to JCPDS No. 17-923 and Murugavel et al. [14], the diffraction pattern corresponds to that of the tetragonal (*T*) phase of the oxide having unit cell parameters $a = 5.0922$ Å and $b = 5.1958$ Å. Broad lines imply that small crystallite sizes were formed in the sample upon heating at 500°C. The average crystallite size was estimated at 5.6 ± 0.4 nm using the Debye–Scherrer equation for the maximum intensity line. Spectra *2* and *3*, which were recorded for zirconia samples prepared by pyrolysis of hydrated zirconia (ZrO_2(p.h.)) and zirconium nitrate (ZrO_2(p.n.)), respectively, correspond to the spectra of the monoclinic (**M**) phase having the parameters $a = 5.3165$ Å, $b = 5.187$ Å, $c = 5.1445$ Å, $\beta = 99.151°$ (Cf. JCPDS No. 36-420). The respective crystallite sizes are 8 and 20 nm.

Figure 1b shows the X-ray diffraction patterns for $Zr_{0.5}Ce_{0.5}O_2$, CeO_2 (m.e.), and CeO_2(p.n.) samples. Both individual oxides have a fluorite-type cubic structure [18]. Reflections for the $Zr_{0.5}Ce_{0.5}O_2$ sample (spectrum *1*) shift toward greater angles relative to their positions in the CeO_2(m.e.) and CeO_2(p.n.) samples (spectra *2*, *3*, respectively), and there is a small line split signifying the presence of the tetragonal phase. The great line width kept us from determining

unit cell parameters exactly, but we still estimated the parameter a at 5.295 Å for the cubic phase of $Zr_{0.5}Ce_{0.5}O_2$ for comparison with literature data. This value is smaller than the unit cell parameter of CeO_2(m.e.) (5.407 Å) or CeO_2(p.n.) (5.412 Å). The aforementioned values are characteristic of nanoparticles [28]. The decrease in unit cell parameter as a result of the replacement of Ce^{4+} cations (having an ionic radius of 0.97 Å) by Zr^{4+} cations (which have a smaller ionic radius of 0.84 Å), agrees with the Vegard rule and indicates the formation of $Zr_{0.5}Ce_{0.5}O_2$ solid solution [18, 29]. The crystallite size in $Zr_{0.5}Ce_{0.5}O_2$ and CeO_2(m.e.) samples is 5.2 nm, while for CeO_2(p.n.) this value is 8.4 nm.

The crystallite size in ZrO_2(m.e.), CeO_2(m.e.), and $Zr_{0.5}Ce_{0.5}O_2$ samples is 5–6 nm, which agrees with X-ray diffraction and TEM data [13, 18, 28]. These data also show that crystallites have spherical shapes and a rather uniform size distribution. The spherical particles model was used to estimate the specific surface area from S (m^2/g) $= 6 \times 10^3/(LD_x)$, where D_x (g/cm^3) is X-ray density and L (nm) is crystallite size. For ZrO_2 having $D_x \approx 5.9$ g/cm^3 and $L = 5.6$ nm, $S =$ 181 m^2/g; for CeO_2 having $D_x \approx 7.2$ g/cm^3 and $L =$ 5.2 nm, $S = 160$ m^2/g. The values calculated differ from the BET surface area values S_{BET} by a factor of 1.6 and 2, respectively (Table 1). This difference is due to the agglomeration of crystallites to sizes of 50–100 nm, as Martinez-Arias et al. observed in $Zr_{0.5}Ce_{0.5}O_2$(m.e.) [18].

Thus, microemulsion technology makes it possible to obtain $Zr_{0.5}Ce_{0.5}O_2$, CeO_2, and ZrO_2 samples having smaller crystallite sizes (5–6 nm) than for the samples prepared by decomposition of nitrate salts and hydroxides (≥8 nm). ZrO_2(m.e.) contains the T phase, as distinct from the M phase contained in ZrO_2 samples prepared by pyrolysis. The CeO_2 samples, regardless of the preparation method, crystallize in the C phase with identical unit cell parameters. Doping CeO_2 with Zr cations produces a $Zr_{0.5}Ce_{0.5}O_2$ solid solution, which likely has a pseudocubic phase and a unit cell parameter intermediate between the CeO_2 and ZrO_2(m.e.) unit cell parameters.

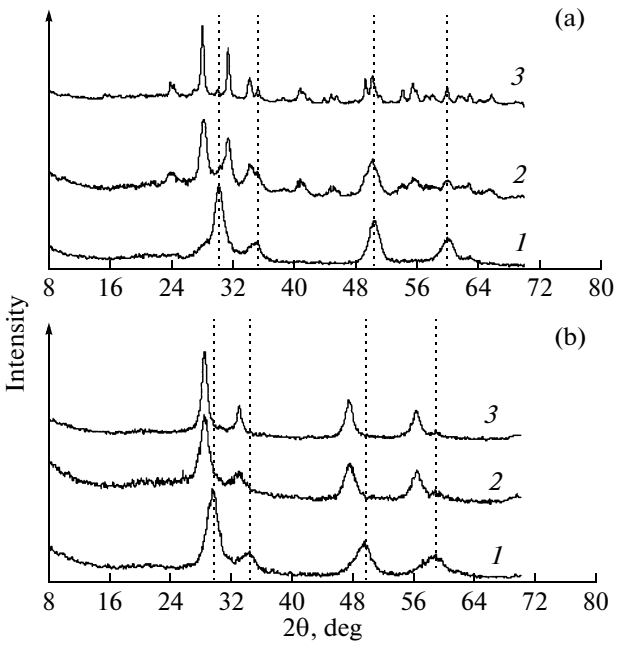

Fig. 1. X-ray diffraction patterns of (a) (*1*) ZrO_2(m.e.), (*2*) ZrO_2(p.h.), and (*3*) ZrO_2(p.n.); (b) (*1*) $Zr_{0.5}Ce_{0.5}O_2$, (*2*) CeO_2(m.e.), and (*3*) CeO_2(p.n.).

Reduction of ZrO_2, CeO_2, and $Zr_{0.5}Ce_{0.5}O_2$ Samples with Hydrogen in the TPR Mode

Figure 2 shows TPR profiles for ZrO_2, CeO_2, and $Zr_{0.5}Ce_{0.5}O_2$(m.e.) samples. Spectrum *1* (for ZrO_2) features a single hydrogen uptake peak at $T_{max} =$ 326°C. Spectrum *2* (for CeO_2) features a high-intensity peak at $T_{max} = 270$°C and an additional peak at 345°C. Spectrum *3* (for $Zr_{0.5}Ce_{0.5}O_2$) has a single peak at $T_{max} = 376$°C. The hydrogen uptake N (molecule/g) and the fraction of surface oxygen that has reacted with hydrogen (R) are compiled in Table 2. R was determined as $R = N/N_o \times 100\%$ (where $N_o = 0.7 \times 10^{19} S_{BET}$, ion/g, is the amount of oxygen ions on the oxidized surface based on the oxide stoichiometry). R being less than 100%, H_2 is likely oxidized only by part of the surface oxygen of the oxides, and bulk oxygen is not involved in the reaction at these temperatures. For

Table 1. Phase composition and particle size characteristics of samples

Sample preparation method	Sample	Phase composition* (X-ray diffraction data)	L, nm	S_{BET}, m^2/g
Emulsion	ZrO_2 (m.e.)	T	5.6	110
Emulsion	CeO_2 (m.e.)	C	5.2	85
Emulsion	$Zr_{0.5}Ce_{0.5}O_2$ (m.e.)	PC	5.2	110
Pyrolysis of $ZrO_2 \cdot nH_2O$	ZrO_2 (p.h.)	M	8.0	100
Pyrolysis of $ZrO(NO_3)_2 \cdot 2H_2O$	ZrO_2 (p.n.)	M	20	56
Pyrolysis of $Ce(NO_3)_3 \cdot 6H_2O$	CeO_2 (p.n.)	C	8.4	80

* C = cubic, M = monoclinic, T = tetragonal, and PC = pseudocubic.

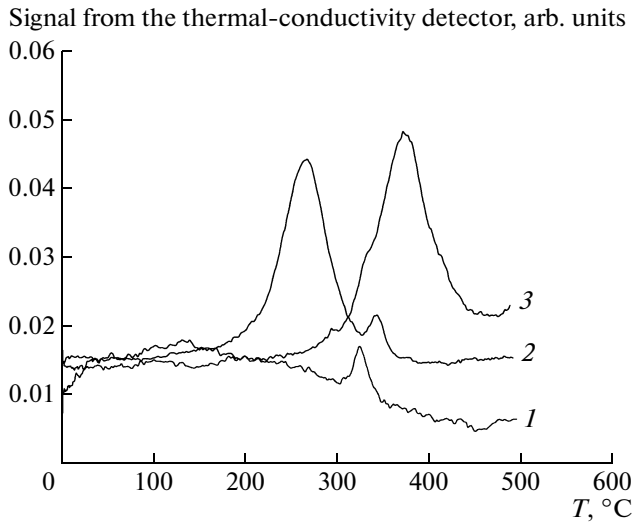

Fig. 2. TPR profiles for (*1*) ZrO_2(m.e.), (*2*) CeO_2(m.e.), and (*3*) $Zr_{0.5}Ce_{0.5}O_2$(m.e.).

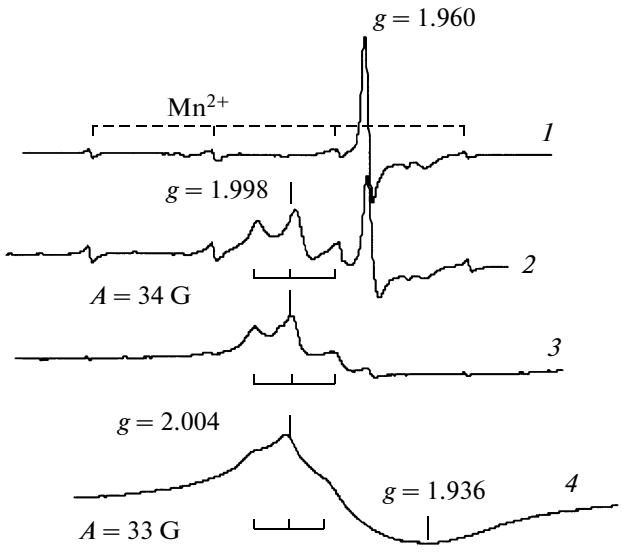

Fig. 3. EPR spectra of (*1*) oxidized CeO_2(m.e.) and (*2–4*) NO adsorbed on (*2*) CeO_2(m.e.), (*3*) $Zr_{0.5}Ce_{0.5}O_2$(m.e.), and (*4*) ZrO_2(m.e.) (vacuum, $T = -196$°C).

ZrO_2, 3% of the reacted oxygen should be assigned to surface defects, while 36–52% of the active oxygen in $Zr_{0.5}Ce_{0.5}O_2$ and CeO_2 samples should be assigned to the surface oxygen of the oxide itself. According to Firsova et al. [30], for CeO_2(p.n.) samples the surface reduction of hydrogen occurs at ~450°C; at ~580°C, nonstoichiometric oxides CeO_x are formed; and at ~920°C, the bulk of CeO_2 is reduced to Ce_2O_3; that is, surface reduction in CeO_2(p.n.) occurs at higher temperatures than in CeO_2(m.e.) (450°C against 270°C). Doping CeO_2 with Zr cations increases the $Zr_{0.5}Ce_{0.5}O_2$ reduction temperature to 370°C, but in this case, too, this temperature remains lower than the reduction temperature of CeO_2(p.n.) or $Zr_{0.5}Ce_{0.5}O_2$ [20, 31].

From these data, it follows that the surface oxygen bond energy on CeO_2 and $Zr_{0.5}Ce_{0.5}O_2$ samples shifts down as the crystallite size decreases (Table 1).

EPR Studies

Lewis acid sites on ZrO_2, CeO_2, and $Zr_{0.5}Ce_{0.5}O_2$ according to NO adsorption data at −196°C. NO adsorption at $T = -196$°C is known to result in the coverage of the oxide surface with physisorbed molecules that form dimeric complexes [32, 33]. On a limited number of low-coordination ions (Lewis acid sites; L^{n+}), molecules are polarized by the field of these sites and form weakly bonded monomeric complexes observable by EPR spectroscopy [23, 34, 35].

Table 2. TPR data for the samples obtained by the microemulsion method

Sample	T_{max}, °C	$H_2 \times 10^4$, mol/g	*R*, %
$Zr_{0.5}Ce_{0.5}O_2$	367	4.4	36
CeO_2	270, 345	4.5, 0.4	48, 4
ZrO_2	326	0.3	3

* *R* is the fraction of surface oxygen reacted with hydrogen.

Figure 3 shows EPR spectra recorded in vacuo for oxidized ZrO_2, CeO_2, and $Zr_{0.5}Ce_{0.5}O_2$ samples after NO absorption (1.2×10^{20} molecule/g) at −196°C. Spectrum *1*, which was recorded for ceria before NO adsorption, features lines from Mn^{2+} uncontrolled impurity ions ($I = 5/2$) and an anisotropic defect line with $g = 1.960$. The nature of this line is yet unclear, although this signal was observed by some researches and discussed in a detailed way by Soria et al. [36]. Spectrum *2* (from NO adsorbed on CeO_2) is has an axial-symmetrical form with $g_\perp = 1.998$, $g_\parallel = 1.865$, and $A_\perp = 34$ Gs. The line with $g_\parallel$ lies in high fields, is masked by one of the Mn lines, and is not indicated in Fig. 3. The characteristic triplet is due to the interaction of the unpaired electron with the nitrogen nuclear spin ($I = 1$) in a molecule. Spectrum *4* recorded for NO molecules on ZrO_2 has $g_\perp = 2.004$, $g_\parallel = 1.936$, and $A_\perp = 33$ Gs. The triplet is practically absent in this spectrum. Spectrum *3* recorded for NO adsorbed on the mixed oxide is similar to the spectrum of NO on CeO_2.

As derived from the EPR spectra of NO adsorbates, the density of Lewis sites (equal to $(1–5) \times 10^{18}$ g^{-1}) is one order of magnitude lower than the density of adsorbate NO molecules and does not exceed 1% of the surface cations. Comparing spectra *1–3*, one can also see that the intensity of the defect lines changes only weakly upon NO admission, probably, because of the inaccessibility of defect locations to adsorbate

molecules. Doping CeO_2 with Zr cations decreases paramagnetic impurity particles likely because of the strong effect of Zr cations on the electronic properties of CeO_2.

Therefore, the oxidized surface of the oxides prepared by the microemulsion method bears Lewis acid sites. The spectra of NO molecules adsorbed on these sites depend both on the oxide cation and on the reciprocal influence of the cations in the mixed oxide. Similar trends were obtained for ZrO_2, CeO_2, and CeO_2/ZrO_2 samples prepared by pyrolysis [23].

EPR from oxygen absorbed on ZrO_2, CeO_2, and $Zr_{0.5}Ce_{0.5}O_2$ is useful to gain more data on coordinatively unsaturated cations.

O_2^- formation upon NO + O_2 and CO + O_2 adsorption on ZrO_2, CeO_2, and $Zr_{0.5}Ce_{0.5}O_2$. O_2 or NO adsorption on oxidized ZrO_2, CeO_2, and $Zr_{0.5}Ce_{0.5}O_2$ does not give rise to an EPR signal. A signal appears after consecutive adsorption of first NO and then O_2 or upon joint adsorption of their mixtures on ZrO_2 and CeO_2 at room temperature, but is not observed for $Zr_{0.5}Ce_{0.5}O_2$. EPR spectra for ZrO_2 and CeO_2 samples are shown in Fig. 4a and Fig. 4b, respectively. They were recorded following NO adsorption (p = 60 Pa) and O_2 adsorption (p = 700 Pa) at 20°C for 3 min, pumping out, and cooling to −196°C. The spectrum for ZrO_2(m.e.) has an anisotropic shape with g_{zz} = 2.035, g_{yy} = 2.008, and g_{xx} = 2.003 (Fig. 4a). This spectrum corresponds to the spectrum of O_2^- radical anions bound by an ionic bond with Zr^{4+} coordinatively unsaturated cations, as we demonstrated earlier for ZrO_2(p.n.) and ZrO_2(p.h.) samples [21, 22]. This bond is sufficiently strong. Experiments on O_2^- (NO + O_2) decomposition to ZrO_2(m.e.) in the range from 20 to 350°C in vacuo support this observation. It was only after the sample was heated at 350°C for 10 min that the density of radical anions decreased from 1×10^{18} g^{-1} to zero.

Figure 4b makes it clear that spectrum *1* for CeO_2(m.e.) has a complex pattern and is similar to spectrum *2* for CeO_2(p.n.), which has a better resolution than spectrum *1*. The spectra correspond to several types of O_2^- radical anions. High-intensity lines having g_{zz} = 2.036, g_{yy} = 2.019, and g_{xx} = 2.011 in spectrum *1* should be assigned to radical anions located in the coordination spheres of coordinatively unsaturated Ce^{4+} cations, and low-intensity satellites having g^1_{zz} = 2.054, g^1_{yy} = 2.008, g^1_{xx} = 2.005 and g^2_{zz} = 2.040, g^2_{yy} = 2.011, g^2_{xx} = 2.008 arise from O_2^- radical anions that are located in the coordination spheres of cations having enhanced electronic densities and different coordination modes of $Ce^{(4-\alpha)+}$ [23]. Earlier [24], we observed that the g_{zz} tensor parameter for O_2^- changed

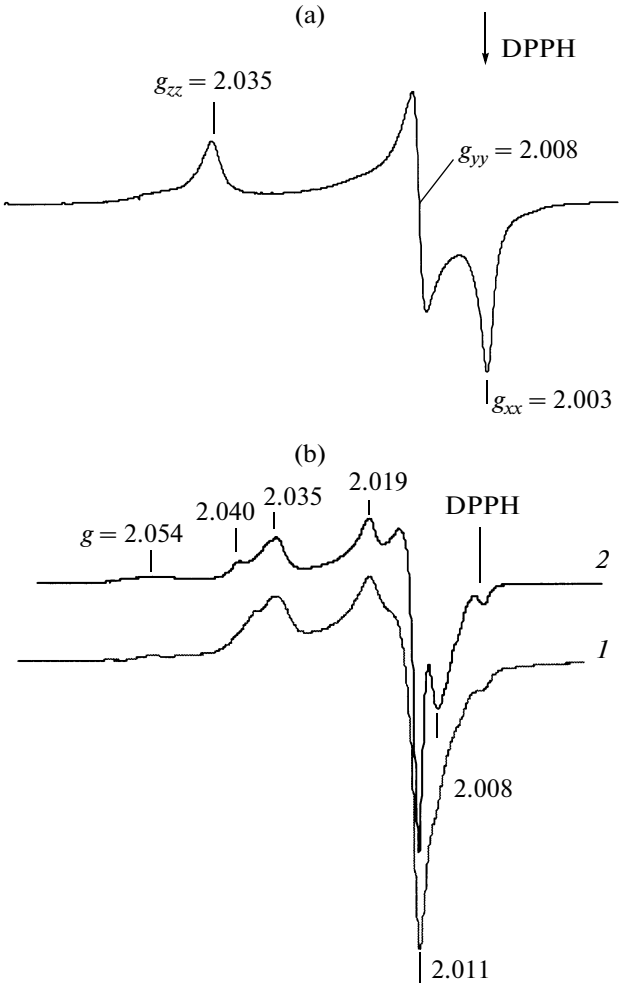

Fig. 4. EPR spectra of oxidized samples recorded at T = −196°C after NO + O_2 adsorption and pumping at 20°C: (a) ZrO_2(m.e.); (b) (*1*) CeO_2(m.e.) and (*2*) CeO_2(p.n.).

by a value close to $g^1_{zz} - g^2_{zz}$ = 0.14 as a result of an alteration of coordination of the complex-forming Ce cation upon CO adsorption [24]. Therefore, mainly O_2^-–Ce^{4+} complexes and a small amount of O_2^-–$Ce^{(4-\alpha)+}$ complexes are formed on the CeO_2(m.e.) surface on cations in different coordination modes. Some O_2^- radical anions on CeO_2(m.e.) were unstable at room temperature. Their amount decreased by a factor of 2.8 from 11×10^{17} g^{-1} at p = 30 Pa to 4×10^{17} g^{-1} upon 10-min evacuation, whereas for CeO_2(p.n.), the amount of the radical anions under similar conditions changed as little as by a factor of ~1.5 from 19×10^{17} g^{-1} to 13×10^{17} g^{-1}. O_2^- species disappear completely upon heating samples in vacuo at 100°C. Bonding in (O_2^-–Ce^{4+}) and (O_2^-–$Ce^{(4-\alpha)+}$) complexes is ionic–covalent, as the values of g_{xx} for O_2^- are greater than the value of the electron g_e-factor, and this differ-

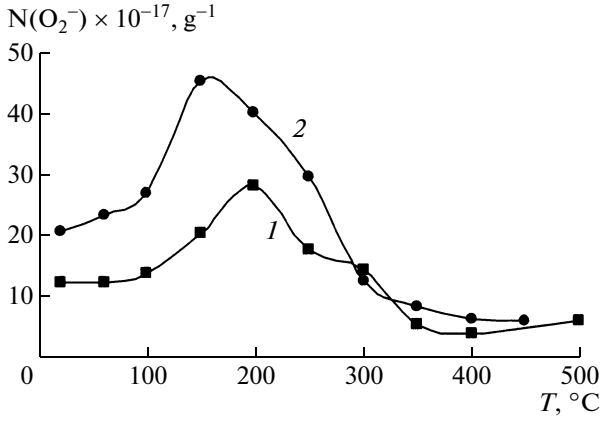

Fig. 5. $O_2^-(CO + O_2)$ concentration as a function of the CO adsorption temperature for oxidized (*1*) CeO_2(m.e.) and (*2*) CeO_2(p.n.).

ence cannot be explained in terms of the ionic model. This difference arises from the formation of a covalent bond via overlapping of the oxygen π_y orbital with the 4*f* orbital of the cation, the latter having a greater spin-orbital coupling constant λ [25, 36].

Consecutive or joint adsorption of CO (5–60 Pa) and oxygen (30–700 Pa) at 20°C generates O_2^- radical anions in the coordination spheres of Ce^{4+} and $Ce^{(4-\alpha)+}$ cations on the oxidized surfaces of CeO_2(m.e.) and CeO_2(p.n.) samples. The EPR spectra of the radical anions were similar to the spectra shown in Fig. 4b. On ZrO_2 and $Zr_{0.5}Ce_{0.5}O_2$ samples, O_2^- radical anions were not detected under these conditions.

Il'ichev et al. [24] and Ismailov et al. [25] noted that $O_2^-(CO + O_2)$ formation on CeO_2(p.n.) is a reaction activated by CO adsorption. This effect was studied in a more detailed way as follows: An oxidized sample was heated to a chosen temperature (T_{CO}), CO was admitted to the sample at 60 Pa, exposed to CO for 10 min, and evacuated. Then, the sample was cooled to room temperature, oxygen was admitted at 700 Pa, the O_2^- spectrum was recorded at an oxygen pressure of 30 Pa to avoid signal broadening because of dipole–dipole interactions, and O_2^- concentration was derived from the EPR spectrum. After recording the spectrum, the sample was oxidized with oxygen at 500°C for 10 min, CO treatment was repeated at another T_{CO}, oxygen was again admitted, and the next spectrum was recorded. Figure 5 shows the $O_2^-(CO + O_2)$ amount as a function of the CO adsorption temperature (T_{CO}) on CeO_2(m.e.) and CeO_2(p.n.) samples. Clearly, the O_2^- concentration on CeO_2(m.e.) increases with rising $T_{CO,}$ to reach a maximal value of 2.5×10^{18} g^{-1} at 200°C, then decreases to acquire a steady-state value of 1.5×10^{18} g^{-1} in the range 250–300°C, and then drops to 5×10^{17} g^{-1} at $T > 400$°C. A similar trend is observed for a CeO_2(p.n.) sample, but in this case the O_2^- concentration at 150°C is approximately twice the maximal O_2^- concentration on the CeO_2(m.e.) sample.

Two schemes of O_2^- formation are operative in the range of the CO adsorption temperatures studied. From 20 to ~200°C O_2^- is generated by electron transfer from electron-donor CO complexes to adsorbate oxygen molecules [24, 25]. In this case, the rise in O_2^- concentration in response to increasing T_{CO} is caused by increasing concentration of CO complexes. IR spectroscopy shows that such complexes may be carbonates or carboxylates [37]. The amount of carbonate and carboxylate complexes decreases when $T_{CO} >$ 200°C, which is likely responsible for the decrease in O_2^- concentration. This is the temperature range where the sample is reduced in CO. The sample changes color from light yellow to light gray at 300°C, and then it turns dark gray at 500°C. The reduced sample is oxidized at 20°C, its color changing to light yellow with the simultaneous generation of O_2^- radical anions. In this case, O_2^- radical anions are generated by the interaction of oxygen molecules with reduced cations in anionic vacancies. The likely reason for the decrease in O_2^- concentration as the CO reduction temperature rises is the conversion of part of the radical anions to O_2^{2-} and O^{2-} nonparamagnetic species, which participate in oxidation of the sample [38]. Further evidence in favor of the occurrence of these redox processes in CO and O_2 is that O_2^-–Ce^{4+} complexes having $g_{zz} =$ 2.034, $g_{yy} = 2.016$, and $g_{xx} = 2.011$ are the only species formed on the reduced surface. Such weakly bonded complexes are completely destroyed upon oxygen evacuation and are reversibly reduced when oxygen is admitted to the sample at room temperature.

The abode data imply that our synthesized ZrO_2(m.e.) and CeO_2(m.e.) samples are active in electron transfer reactions. Identical reaction parameters, radical-anion stabilization schemes, and thermal stability of O_2^- are indicative of identical reaction schemes for oxides that have different particle sizes in the nanometer range. However, the oxides synthesized by microemulsion technology have activities one-half to one-third the activities of oxides synthesized by pyrolysis.

O_2^- formation upon oxygen adsorption on $Zr_{0.5}Ce_{0.5}O_2$, ZrO_2(m.e.), and CeO_2(m.e.) samples reduced in CO and H_2. Inasmuch as oxidized $Zr_{0.5}Ce_{0.5}O_2$ was inactive in electron transfer reaction during $NO + O_2$ and $CO + O_2$ adsorption, we studied

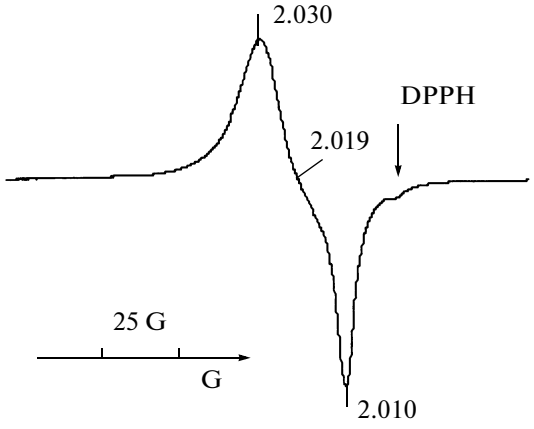

Fig. 6. EPR spectrum of $Zr_{0.5}Ce_{0.5}O_2$ recorded at $T = -196$°C in vacuo after oxygen adsorption on the sample prereduced with hydrogen at 500°C.

oxygen adsorption on a reduced sample. Once oxygen ($p = 700$ Pa, $T = 20$°C) was admitted to a $Zr_{0.5}Ce_{0.5}O_2$ sample that had been reduced in H_2 or CO ($p = 70$ Pa, $T = 500$°C, $\tau_r = 10$ min), a small EPR signal was recorded. Its intensity increased tenfold as the temperature of the sample was lowered to ~10°C. This signal corresponds to reversible weakly bound oxygen adsorbate species, as it disappears upon oxygen evacuation and is reversible reduced when oxygen is admitted to the sample. Figure 6 shows the EPR spectrum for a hydrogen-reduced sample after admission of O_2 at 20°C, cooling to −196°C, and pumping out. This spectrum differs from the O_2^- spectra recorded on ZrO_2(m.e.) and CeO_2(m.e.) (Figs. 4a, 4b). However, the values of parameters $g_{zz} = 2.030$, $g_{yy} = 2.019$, and $g_{xx} = 2.010$ and the spectral intensity as a function of oxygen pressure enable us to assign this spectrum to O_2^-–Ce^{4+} paramagnetic complexes. A similar adsorbate oxygen complex was observed on a sample prereduced in CO. A similar EPR signal of O_2^- was detected upon oxygen adsorption on CeO_2/ZrO_2 [24] and CeO_2/Al_2O_3 [39] supported catalysts. The authors believe that the decreased O_2^-–Ce^{4+} bond strength on the supported samples relative to undoped CeO_2 signifies strong interactions of cations; one more manifestation of this interaction is an alteration of the O_2^- spectral pattern. Therefore, O_2^- radical anions are stabilized on the surface of $Zr_{0.5}Ce_{0.5}O_2$ only on Ce coordinatively unsaturated cations, which interact with zirconium cations. This interaction enhances the formation of cations having an excess positive charge ($Ce^{(4+\beta)+}$) and a reduced positive charge ($Zr^{(4-\beta)+}$) [28]. The decrease of $g_{zz} = 2.035$ for O_2^-–Ce^{4+} complexes to $g_{zz} = 2.030$ is likely due to the stabilization of O_2^- in the coordination sphere of $Ce^{(4+\beta)+}$ cations.

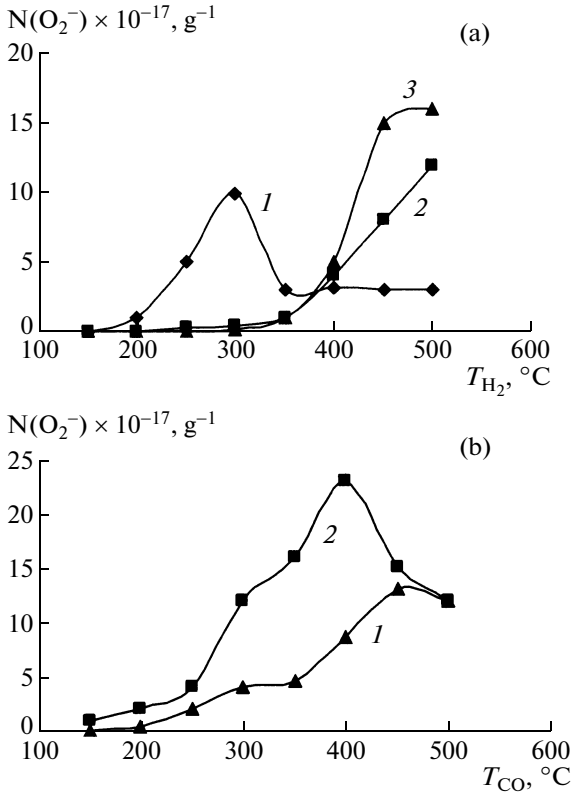

Fig. 7. O_2^- concentration in oxides after oxygen adsorption as a function of temperature: (a) (*1*) CeO_2(m.e.), (*2*) ZrO_2(m.e.), and (*3*) $Zr_{0.5}Ce_{0.5}O_2$(m.e.) prereduced with hydrogen; (b) (*1*) ZrO_2(m.e.) and (*2*) $Zr_{0.5}Ce_{0.5}O_2$(m.e.) prereduced with CO.

In reduced ZrO_2(m.e.) and CeO_2(m.e.) samples, O_2^- was detected under similar conditions upon oxygen adsorption. Regardless of the nature of the reducing agent, the thermal stability and parameters of O_2^- radical anions on ZrO_2 coincide with those for O_2^- ($NO + O_2$). For O_2 on CeO_2(m.e.), O_2^- radical anions were observed on Ce^{4+} and $Ce^{(4-\delta)+}$ cations, which also corresponded to $O_2^-(NO + O_2)$; after reduction in CO, only O_2^- on Ce^{4+} were observed, as mentioned above.

Figure 7a shows O_2^- concentration as a function of hydrogen reduction temperature ($p = 70$ Pa, $\tau_r = 10$ min) for CeO_2(m.e.), ZrO_2(m.e.), and $Zr_{0.5}Ce_{0.5}O_2$(m.e.) samples. Reduction of CeO_2 (curve *1*) in H_2 starts at 200°C, while ZrO_2 and $Zr_{0.5}Ce_{0.5}O_2$ are reduced starting at 300°C (curves *2*, *3*). These results agree with the TPR data. The extreme character the O_2^- amount as a function of the CeO_2 reduction temperature is due to the increasing rate of O_2^- conversion to nonparamagnetic oxygen adsorbate species as the degree of reduction of the sample

increases. The change in color from lemon to dark gray proves the greater degree of reduction in hydrogen.

For ZrO_2(m.e.) and $Zr_{0.5}Ce_{0.5}O_2$ samples, O_2^- concentration was also determined as a function of the reduction temperature in CO. Figure 7b makes it clear that the mixed oxide is likely to be reduced more easily than zirconia. We must note that the onset reduction temperature in CO is ~100 K lower than in hydrogen (Figs. 7a, 7b).

DISCUSSION

Structure Formation in Oxides Prepared by Microemulsion Method

Experimental data show that the microemulsion synthesis and the standard precipitation method in aqueous solutions yield ZrO_2 as the *T* and *M* phase, respectively. Despite the similarity of the methods, precursors formed in their gels differ from each other in both particle sizes and structures. According to the idea of a critical particle size of ZrO_2 [8, 13], for crystallite sizes less 10 nm, the formation of the *T* phase is energetically more preferred than the formation of the *M* phase. The crystallite size is controlled by the precursor particle size in gel. Apparently, crystallites of the *T* phase having sizes of 5–6 nm are formed from gel microparticles, whereas particles of the *M* phase are formed from $ZrO_2 \cdot nH_2O$ polyoxo complexes [29]. Apart from the size effect, Ward and Ko [16] think that the formation of the *T* phase from an amorphous gel phase is more preferred than the formation of the *M* phase, as the amorphous phase and the *T* phase have identical short-range orders. In this case, it is expected that the energy barrier to the transition from the amorphous to tetragonal phase is lower than for the transition from the amorphous to monoclinic phase.

Stabilization of the *T* phase in ZrO_2 was observed when the sample was doped with Y^{3+} and Ca^{2+} in a certain concentration [40, 41] and in the presence of SO_4^{2-} and Cl^- anions of $Zr(SO_4)_2$ and $ZrOCl_2$ precursors [42]. In our case, it is unlikely that Cl^- ions stabilize the *T* phase. Firstly, the *T* phase was not detected in ZrO_2(p.h.) (Fig. 1a). Secondly, the influence of Cl^- ions was not manifested in the EPR spectra of O_2^- radical anions in the samples studied regardless of the way the spectrum was generated. Thirdly, the *M* phase was not found in ZrO_2(m.e.) after the sample was repeatedly subjected to oxidation/reduction treatment at 500°C under vacuum, where Cl removal from the sample should be accompanied by conversion of the *T* phase to *M* phase according to Benfer and Knozinger [13]. This is the basis to suggest that Cl^- ions play only a subordinate role in the formation of the *T* phase during ZrO_2(m.e.) synthesis, and the major cause of its stabilization consists in the properties of the precursor in the precipitated gel.

Hydrogen oxidation by surface oxygen on ZrO_2(m.e.) in the TPR mode is due to a small amount of surface oxygen sites, which constitute 3% of the surface oxygen of the oxide and are likely bound to defects. The reduction of these sites in hydrogen and a subsequent reaction with oxygen generate O_2^- radical anions (Fig. 7a). ZrO_2(p.n.) and ZrO_2(p.h.) samples are not reduced by hydrogen at 20–600°C, and radical anions are not formed during oxygen adsorption that follows this treatment [21]. Likely, these defects in ZrO_2(m.e.) are generated during synthesis at the step of heat treatment in air. More studies are needed to elucidate their nature.

Doping ZrO_2 with cerium cations during microemulsion synthesis provides a sufficiently homogeneous phase in a $Zr_{0.5}Ce_{0.5}O_2$ sample without ZrO_2 and CeO_2 impurity phases, as probed by X-ray diffraction. The absence of ZrO_2 and CeO_2 impurities in the mixed oxide is verified by its inactivity in electron transfer reactions during NO + O_2 and CO + O_2 adsorption. The pseudocubic phase of the $Zr_{0.5}Ce_{0.5}O_2$ sample should be assigned to the tetragonal (*T*) phase having the unit cell parameters $a \approx c$ and space group $P4_2/nmc$ [8]. The split of lines in the X-ray diffraction patterns of this sample also indicates the existence of this phase. Raman spectroscopy verified the existence of this phase in a $Zr_{0.5}Ce_{0.5}O_2$ sample synthesized by the microemulsion method [18].

Fally et al. [31] observed a shift down of the surface reduction temperature in hydrogen from 627 to 300°C as crystallite sizes in ZrO_2–CeO_2 samples decreased. In our case, the $Zr_{0.5}Ce_{0.5}O_2$ surface reduction temperature in hydrogen for crystallite sizes of 5–6 nm corresponds to $T_{max} = 360$°C (Figs. 2, 7a) and nicely agrees with the data of Fally et al. data and those of Rodriguez et al. [28]. The different reduction temperatures for CeO_2 samples prepared by the microemulsion method (270°C) and those prepared by pyrolysis (450°C) also arise from different crystallite sizes.

Properties of Surface Sites of ZrO_2, CeO_2, and $Zr_{0.5}Ce_{0.5}O_2$ Prepared by the Microemulsion Method

The oxidized surfaces of ZrO_2, CeO_2, and $Zr_{0.5}Ce_{0.5}O_2$ bear Lewis acid sites whose concentration, as probed by EPR, does not exceed ~1% of the total amount of the surface cations.

The nature of Lewis sites of the mixed oxide is an interesting point of discussion. $Zr_{0.5}Ce_{0.5}O_2$ has surface properties differing from the properties of ZrO_2 and CeO_2 samples. The interactions of Zr and Ce cations make its oxidized surface inactive in the electron-transfer reaction during NO + O_2 and CO + O_2

adsorption. Specific O_2^- radical anions having low thermal stability were observed on the reduced surface, these radical anions being likely located on $Ce^{(4+\beta)+}$ cations. Ionically bonded O_2^-–Zr^{4+} complexes have not been detected possibly because of an altered charge state of Zr cations [28] or location of Zr cations in the near-surface layer, which is inaccessible to dioxygen adsorption. TPR data argue in favor of the second suggestion. Figure 2 makes it clear that the bond energy of surface oxygen in CeO_2 increases as CeO_2 is doped with Zr cations, but its amount remains practically unchanged. The coincidence of the EPR spectra from NO adsorbates on CeO_2 and $Zr_{0.5}Ce_{0.5}O_2$ may serve as another argument in favor of this suggestion (see Fig. 3).

ZrO_2(m.e.) and CeO_2(m.e.) samples are both active in the electron transfer reaction to yield O_2^- ($NO + O_2$) radical anions, and CeO_2 is in addition active in the reaction that yields O_2^-($CO + O_2$). The two- to threefold decrease in their activity compared to the analogues synthesized by pyrolysis likely arises from a reduced density of reaction sites and indicates a lower defect density in ZrO_2(m.e.) and CeO_2(m.e.) samples. The reaction scheme is independent of the crystallite size. This implies that the reaction on the surface of ZrO_2(m.e.) and CeO_2(m.e.) samples also proceeds on M^{4+}–O^{2-} coordinatively unsaturated pairs (where M = Zr or Ce cation), as in their analogues prepared by pyrolysis [21, 23]. Adsorption of NO and CO on these pairs produces electron-donor complexes (chelate complexes for NO and carbonate and carboxylate complexes for CO). Electron transfer from these complexes to molecular oxygen adsorbates gives rise to O_2^- radical anions, which are stabilized by ionic and ionic–covalent bonds in the coordination spheres of Zr and Ce cations, respectively.

Surface sites on ZrO_2 samples having different phase compositions are known to have different reactivities [43]. In the case at hand, the spectral characteristics of O_2^-–Zr^{4+} complexes and their thermal stability had close values for samples having *T* and *M* phases. Therefore, the ionic bond strength in an O_2^-–Zr^{4+} pair is unaffected by the phase composition of the oxide.

The reduction of ZrO_2 and $Zr_{0.5}Ce_{0.5}O_2$ samples in CO starts at lower temperatures than in hydrogen (Figs. 7a, 7b). For CeO_2, testing the initial stage of surface reduction in CO by measuring the O_2^- amount formed upon O_2 adsorption was inefficient because of two possible schemes of radical anion generation. At $T < 200$°C, the process involves electron transfer between CO and oxygen adsorbate complexes; when $T > 200$°C, it involves the interaction of O_2 with sites that have been reduced in CO. The existence of a temperature range where both O_2^- generation schemes are operative cannot rule out that CO oxidation by oxygen radical anions follows a joint scheme, which is energetically more preferred than an alternation of surface reduction and oxidation that comes into play at elevated temperatures [44]. In the latter case, radical anions can be intermediates of the oxidation reaction, transforming on the reduced surface from O_2^- paramagnetic oxygen adsorbates to O^{2-} ionic species as follows: $O_2 \longleftrightarrow O_2^- \longleftrightarrow O_2^{2-} \longleftrightarrow O^- \longleftrightarrow O^{2-}$ [45].

Acidity of Lewis Surface Sites of Oxides

The EPR spectra of NO adsorbed at −196°C on ZrO_2, CeO_2, and $Zr_{0.5}Ce_{0.5}O_2$(m.e.) samples are similar to the spectra of NO on ZrO_2, CeO_2, and 10% CeO_2/ZrO_2(p.h.) and (p.n.) samples obtained in [23], and they depend on the nature of the Lewis site (L^{n+}) with which an NO molecule forms a donor–acceptor bond L^{n+}–$N^- = O^+$. As the acidity of the cation increases, the L^{n+}–N^- bond strength increases, too, but the unpaired electron density on the nitrogen atom decreases because of being displaced to the oxygen atom. This leads to a decrease in the separation between HFS lines [35]. For this reason, HFS lines are better resolved in the EPR spectra of NO adsorbed on cerium cations than for NO adsorbed on zirconium cations at −196°C (see Fig. 3). Based on this, we may suggest that ZrO_2 has a higher acidity than CeO_2, and CeO_2 and $Zr_{0.5}Ce_{0.5}O_2$ have close acidities; that is, $ZrO_2 > CeO_2 \approx Zr_{0.5}Ce_{0.5}O_2$. A similar acidity order was derived from IR spectroscopic studies of CO adsorption on these oxides at $T = -196$°C [46].

Volodin et al. [47] mentioned that the broadening of the EPR spectrum of NO adsorbates is made possible by the mobility of NO adsorbate molecules at elevated temperatures (−130°C) where NO desorption is possible. This scenario is unlikely at −196°C because the bond strength of NO with Zr cations is greater than with Ce cations [46]. An argument in favor of the strong adsorption of molecules is that the intensity and pattern of the spectrum for NO adsorbed on ZrO_2 did not change when recorded repeatedly under continuous evacuation at $T = -196$°C.

Assuming that the bond strength of a probe molecule with a Lewis site correlates with the acidity of the latter, for O_2^- radical anions we obtain the order $ZrO_2 > CeO_2 > Zr_{0.5}Ce_{0.5}O_2$, where the O_2 bond strength with oxides decreases from ZrO_2 to $Zr_{0.5}Ce_{0.5}O_2$. From the comparison of the rows, it follows that bonding of both NO molecules and radical anions with zirconium cations in ZrO_2 is higher than with cerium cations in CeO_2. Bonds of NO molecules with cations in CeO_2 and $Zr_{0.5}Ce_{0.5}O_2$ samples have similar values, whereas O_2^- radical anions are more strongly bonded with cations in CeO_2 than in $Zr_{0.5}Ce_{0.5}O_2$. This is indicative of

the occurrence, on the mixed oxide, of some surface sites whose acidity is lower than the acidity of cations in CeO_2. In light of this, the acidity row may be represented as $ZrO_2 > CeO_2 \geq Zr_{0.5}Ce_{0.5}O_2$.

ACKNOWLEDGMENTS

This work was supported by the Russian Foundation for Basic Research, project no. 07-03-01074.

REFERENCES

1. He, M.Y. and Ekerdt, J.G., *J. Catal.*, 1984, vol. 87, p. 381.
2. Domen, K., Koodo, J., Maruya, K., and Onishi, T., *Catal. Lett.*, 1992, vol. 12, p. 127.
3. Nakano, Y., Yamaguchi, T., and Tanabe, K., *J. Catal.*, 1983, vol. 80, p. 307.
4. Monteiro, A.M., Sapina, F., Martinez, E., Corberan, V.C., and Rangel, M.C., *Proc. EuropaCat IX*, Salamanca, Spain, 2009, p. 8-14.
5. Sakura, T., Sakata, Y., and Imamura, H., *Proc. EuropaCat IX*, Salamanca, Spain, 2009, p. 3-96.
6. Daturi, M., Bion, N., Saueeey, J., Hedouin, C., Segueiong, T., and Blanchard, G., *Phys. Chem. Chem. Phys.*, 2001, vol. 3, p. 252.
7. Kaspar, J., Fornasiero, P., and Hickey, N., *Calal. Today*, 2003, vol. 77, p. 419.
8. Fornasiero, P., Balducci, G., Di Monte, R., Kaspar, J., Sergo, V., Gubitosa, G., Ferrero, A., and Graziani, M., *J. Catal.*, 1996, vol. 164, p. 178.
9. Martinez-Arias, A., Fernandez-Garcia, M., Galvez, O., Coronado, J.M., Anderson, J.A., Conesa, J.C., Soria, J., and Munuera, G., *J. Catal.*, 2000, vol. 195, p. 207.
10. Martinez-Arias, A., Fernandez-Garcia, M., Hungria, A.B., Iglesias-Juez, A., Galvez, O., Anderson, J.A., Conesa, J.C., Soria, J., and Munuera, G., *J. Catal.,* 2003, vol. 214, p. 261.
11. Ratnasamy, P., Srinvas, D., Satyanarayana, C.V.V., Manikandan, P., Senthil Kumaran, R.S., Sachin, M., and Shetti, V.N., *J. Catal.*, 2004, vol. 221, p. 455.
12. Iglesia, E., *Proc. EuropaCat IX*, Salamanca, Spain, 2009, p. 1-1.
13. Benfer, S. and Knozinger, E., *J Mater. Chem.*, 1999, vol. 9, p. 1203.
14. Murugavel, P., Kalaiselvam, M., Rajn, A.R., and Rao, C.N.R., *J Mater. Chem.*, 1999, vol. 7, p. 1433.
15. Caracoche, M., Rivas, P.C., and Cervera, M.M., *J. Mater. Res.*, 2003, vol. 18, no. 1, p. 208.
16. Ward, D.A. and Ko, E.I., *Chem. Mater.*, 1993, vol. 5, p. 956.
17. Bedilo, A.F. and Klabunde, K.J., *Nanostruct. Mater.*, 1997, vol. 2, no. 2, p. 119.
18. Martinez-Arias, A., Fernandez-Garcia, M., Ballesteros, V., Salamanca, L.N., Conesa, J.C., Otero, C., and Soria, J., *Langmuir*, 1999, vol. 5, p. 4796.
19. Fornasiero, P., Di Monte, R., Randa, Rao., Kaspar, J., Meriani, S., Trovarelli, A., and Graziani, M., *J. Catal.*, 1995, vol. 151, p. 168.
20. Trovarelli, A., Zamar, F., Llorca, J., de Leitenburg, C., Dolcetti, G., and Kiss, J.T., *J. Catal.*, 1997, vol. 169, p. 490.
21. Il'ichev, A.N., Konin, G.A., Matyshak, V.A., Kulizade, A.M., Korchak, V.N., and Yan, Yu.B., *Kinet. Katal.*, 2002, vol. Vol. 43, no. 2, p. 235 [*Kinet. Catal.* (Engl. Transl), vol. 43, no. 2, p. 214].
22. Il'ichev, A.N., Shibanova, M.D., and Korchak, V.N., *Kinet. Katal.*, 2004, vol. 45, no. 1, p. 126 [*Kinet. Catal.* (Engl. Transl.), vol. 45, no. 1, p. 114].
23. Il'ichev, A.N., Shibanova, M.D., and Ukharskii, A.A., Kuli-zade, A.M., and Korchak, V.N., *Kinet. Katal.*, 2005, vol. 46, no. 3, p. 414 [*Kinet. Catal.* (Engl. Transl.), vol. 46, no. 3, p. 387].
24. Il'ichev, A.N., Kuli-zade, A.M., and Korchak, V.N., *Kinet. Katal.*, 2005, vol. 46, no. 3, p. 423 [*Kinet. Catal.* (Engl. Transl.), vol. 46, no. 3, p. 396].
25. Ismailov, E.G., Maksimov, N.G., Anufrienko, V.F., and Sokolovskii, V.V., *React. Kinet. Catal. Lett.*, 1977, vol. 7, no. 1, p. 99.
26. Jung, K.T. and Bell, A.T., *J. Mol. Catal.*, 2000, vol. 163, p. 27.
27. *Handbuch der preparativen anorganischen Chemie*, von Brauer, G., Ed., Stuttgart: Ferdinand Enke, 1981.
28. Rodriguez, J.A., Hanson, J.C., Kim, J., Liu, G., Iglesias-Juez, A., and Fernandez-Garcia, M., *J. Phys. Chem. B*, 2003, vol. 197, p. 3535.
29. Kuznetsova, T.G. and Sadykov, V.A., *Kinet. Katal.*, 2008, vol. 49, no. 6, p. 886 [*Kinet. Catal.* (Engl. Transl.), vol. 49, no. 6, p. 840].
30. Firsova, A.A., Khomenko, T.N., Il'ichev, A.N., and Korchak, V.N., *Kinet. Katal.*, 2008, vol. 49, no. 5, p. 713 [*Kinet. Catal.* (Engl. Transl.), vol. 49, no. 5, p. 682].
31. Fally, F., Perrichon, V., Vidal, H., Kaspar, J., Blanco, G., Pintado, J.M., Bernal, S., Colon, G., Daturi, M., and Lavalley, J.C., *Catal. Today*, 2000, vol. 59, p. 373.
32. Escalona Platero, E., Spoto, G., and Zecchina, A., *J. Chem. Soc., Faraday Trans. 1*, 1985, vol. 81, p. 1283.
33. Escalona Platero, E., Scarano, D., Spoto, G., and Zecchina, A., *Faraday Discuss.*, 1985, vol. 80, p. 183.
34. Paganini, M.C., Chiesa, M., Martino, P., and Giamello, E., *J. Phys. Chem. B*, 2002, vol. 106, p. 12531.
35. Rudolf, T., Böhlman, W., and Pöppl, A., *J. Magn. Reson.*, 2002, vol. 155, p. 45.
36. Soria, J., Martinez-Arias, A., and Conesa, J.C., *J. Chem. Soc., Faraday Trans.*, 1995, vol. 91, no. 11, p. 1669.
37. Li, C., Sakata, Y., Domon, T.K., Maruya, K., and Oniashi, T., *J. Chem. Soc., Faraday Trans. 1* 1989, vol. 4, no. 4, p. 929.

38. Krylov, O.V. and Kiselev, V.F., *Adsorbtsiya i kataliz na perekhodnykh metallakh i oksidakh* (Adsorption an Catalysis on Transition Metal Oxides), Moscow: Khimiya, 1981.

39. Soria, J., Coronado, J.M., and Conesa, J.C., *J. Chem. Soc., Faraday Trans. 1*, 1996, vol. 92, no. 9, p. 1619.

40. Taraya, H., *J. Am. Ceram. Soc*, 1989, vol. 72, p. 662.

41. Barker, W.W., Baily, F.P., and Garrett, W., *J. Solid State Chem.*, 1973, vol. 7, p. 448.

42. Stefanik, G., Music, S., Porovic, S., and Furle, K., *Croat. Chim. Acta*, 1996, vol. 69, p. 223.

43. Jung, K.T. and Bell, A.T., *Top. Catal.*, 2002, vol. 20, p. 97.

44. Sokolovskii, V.D., Boreskov, G.K., Dovydov, A.A., Gundrizer, T.A., Anufrienko, I.F., Izmailov, E.G., Budnova, A.A., and Maksimov, N.G., *Dokl. Akad. Nauk SSSR*, 1974, vol. 216, no. 3, p. 599.

45. Sedmak, G., Hasevar, S., and Levec, J., *J. Catal.*, 2003, vol. 213, p. 135.

46. Daturi, M., Binet, C., Lavalley, J-C., Galtayries, A., and Sporken, R., *Phys. Chem. Chem. Phys.*, 1999, vol. 1, p. 5717.

47. Volodin, A., Biglino, D., Itagaki, Y., Shiotani, M., and Lund, A., *Chem. Phys. Lett.*, 2000, vol. 327, p. 166.